AIAA SciTech Forum
12-16 January 2026, Orlando, FL
AIAA SCITECH 2026 Forum

10.2514/6.2026-1928

Statistical modeling of energy amplification of inflow perturbations in boundary layer flows

Saarthak Gupta*, James Paulson†, Peter Frame‡, Aaron Towne§
University of Michigan, Ann Arbor, MI 48109, USA

Linear growth of disturbances plays a crucial role in the laminar-to-turbulent transition in boundary layers and other wall-bounded flows. Although the linearized Navier–Stokes operator may be stable in such flows, its non-normality can amplify disturbances significantly, underscoring the importance of characterizing the evolution of realistic perturbations under linear dynamics. Such perturbations typically arise from broadband environmental sources rather than carefully constructed optimal modes, making a statistical description a natural approach for examining their evolution. Recent work has proposed a statistical framework that relates the two-point correlation tensor of the incoming disturbances to the downstream turbulent intensity, assuming linear evolution of the perturbations. This provides a way to predict the average behavior of disturbance fields rather than focusing on specific optimal disturbances. The primary aims of the work are to implement this framework for a Blasius boundary layer and to perform direct numerical simulation (DNS) of the same flow in order to assess the predictions of the statistical framework. To model the statistics of the free-stream turbulence, the inflow disturbances are prescribed using the von Kármán energy spectrum. Applying the statistical framework to a spatially developing flow requires a spatial marching procedure, for which we use the one-way Navier-Stokes equations (OWNS). We also develop a reduced-basis technique to approximate formulae in the statistical framework that would otherwise be intractable for this flow. Finally, we present a comparison of the kinetic energy growth obtained from the DNS with that predicted by the statistical framework at select frequency-spanwise wavenumber pairs, along with a comparison of the disturbance mode shapes predicted by DNS and OWNS.

I. Introduction

Laminar-to-turbulent transition in boundary layer flows remains a fundamental problem of significant technological importance, owing to its influence on skin-friction drag, heat transfer rates, momentum mixing, and flow control. Given these practical implications, considerable research effort has been devoted to understanding and predicting the onset of transition across a wide range of flow conditions [1, 2]. A variety of theoretical and computational frameworks have emerged to tackle this challenge. Linear stability theory [3] provides insight into the growth of infinitesimal disturbances and serves as the foundation for many transition prediction models. The widely used N-factor method [4] estimates transition onset by tracking the exponential amplification of instability waves until a critical threshold is reached. To account for the slow variation of the boundary layer base flow in the streamwise direction, the parabolized stability equations (PSE) [5] offer a framework for computing the spatial growth of disturbance amplitudes. However, PSE has been shown to inadequately capture non-modal amplification mechanisms that are often crucial to boundary-layer transition [6]. To address these limitations, the linear one-way Navier-Stokes (OWNS) marching algorithm [7, 8], derived using inspiration from outflow boundary conditions, enables improved modeling of disturbance evolution in slowly varying flows. Extending this framework, the recently proposed non-linear OWNS (NOWNS) [9] solves for the entire discretized wavenumber-frequency space simultaneously, incorporating non-linear interactions across the wavenumber space. As a result, NOWNS can capture non-parallel, non-modal, and nonlinear instability mechanisms. At the fully nonlinear end of the modeling approaches, direct numerical simulations (DNS) [10–12] provide a comprehensive tool for studying transition by resolving all relevant scales of motion without modeling assumptions, albeit at significant

*Research Fellow, Department of Mechanical Engineering
†Graduate Student, Department of Mechanical Engineering
‡Graduate Student, Department of Mechanical Engineering
§Associate Professor, Department of Mechanical Engineering, AIAA Senior Member

computational cost. These approaches encompass a range of models—from linear to fully nonlinear—that collectively enhance our understanding of transition mechanisms in wall-bounded flows.

Several different mechanisms can lead to transition in boundary-layer flows, depending on factors such as the amplitude and nature of inflow disturbances, surface roughness, and freestream turbulence levels. In low-disturbance-amplitude scenarios, transition typically proceeds via the amplification of Tollmien-Schlichting (TS) waves, linear instability modes of the boundary layer that eventually undergo secondary instabilities and break down to turbulence [2, 3]. In noisy or high-disturbance-amplitude environments, transition can occur through mechanisms that bypass the TS-wave route and do not rely on the exponential growth of the TS waves [13, 14]. In such cases, the non-normality of the linearized Navier-Stokes (LNS) operator can be crucial to the evolution of the disturbances that eventually lead to transition [15, 16]. When the LNS operator is linearly stable, this non-normality allows for substantial transient growth, which can activate nonlinearities and ultimately lead to breakdown. Even if the LNS operator is modally unstable, the transient growth mechanism, which often acts faster than modal growth, can cause transition. While transient growth is most prominently associated with bypass transition, it can distort TS waves [17] and potentially cause transition through a different route.

Standard transient growth analyses study the transient growth mechanism by finding the maximum growth over all initial disturbances. However, real flow disturbances will not happen to coincide with the optimally amplified one. Ref. [18] therefore proposed a statistical framework for studying transient growth. In this framework, inlet disturbances are treated as random variables, and the framework relates the statistics of the downstream disturbances, e.g., the mean and distribution of downstream energy, to those of the inlet disturbances. The framework operates under the assumption of linearity and, in the case of spatial growth, assumes the existence of a spatial marching operator.

The main objectives of the present work are to apply the statistical framework to a Blasius boundary layer and to conduct a DNS to generate results to compare with those from the statistical framework. Applying the framework to the boundary layer requires a one-way formulation of the linearized Navier-Stokes equations, and we use the projection form of OWNS [19], which provides a spatial marching operator. We impose a statistical distribution of disturbances at the inflow of the boundary layer, then use this marching operator to propagate these statistics downstream, studying, in particular, the mean energy growth. We set up a direct numerical simulation of a transitional Blasius boundary layer using the spectral element code Nek5000 [20], again imposing a particular distribution of inflow statistics. The resulting mean energy growth obtained from DNS is compared with predictions from the reduced-order statistical framework, and the corresponding disturbance mode shapes obtained from DNS are compared with those predicted by OWNS.

II. Analysis methods

In this section, we detail the methods used in this paper to study energy amplification in a Blasius boundary layer. In II.A, we provide an overview of the statistical framework and present key formulae for statistics to compare against the DNS. We describe the statistical distribution of inflow disturbances used in both the DNS and the OWNS in II.B. In II.C, we review the linear OWNS equations, which are used to implement the statistical framework. Finally, we provide details of the boundary-layer DNS in II.D.

A. Statistical framework

We consider the linear phase of the streamwise evolution of disturbances Fourier transformed in the spanwise direction and in time. At a particular streamwise location x, spanwise wavenumber β, and frequency ω, a disturbance comprises N_v flow variables at N_y gridpoints in the wall-normal direction and is denoted by $\boldsymbol{q}(x,\beta,\omega) \in \mathbb{C}^{N_v N_y}$. We assume that the downstream disturbance may be related to the inflow disturbance by a linear propagation operator $\boldsymbol{\Pi}(x,\beta,\omega) \in \mathbb{C}^{N_v N_y \times N_v N_y}$ as

$$\boldsymbol{q}(x,\beta,\omega) = \boldsymbol{\Pi}(x,\beta,\omega)\boldsymbol{q}(0,\beta,\omega). \tag{1}$$

The details of obtaining this propagation operator, as well as its relation to the linearized Navier-Stokes equation, are given in Section II.C.

Standard transient growth theory [16, 21, 22] seeks to understand the linear mechanisms for energy growth by finding the optimal growth, defined as

$$G^{opt}(x,\beta,\omega) = \max_{\boldsymbol{q}(0,\beta,\omega)} \frac{\|\boldsymbol{q}(x,\beta,\omega)\|^2}{\|\boldsymbol{q}(0,\beta,\omega)\|^2} \tag{2}$$

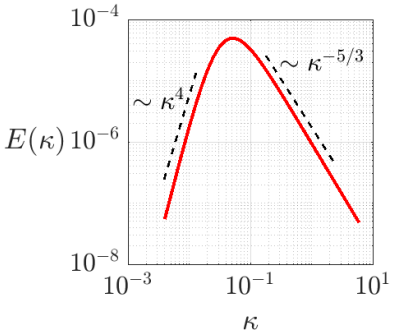

Fig. 1 One-dimensional von Kármán energy spectrum, $E(\kappa)$, computed using Eq. (7) for turbulent intensity, $TI = 0.25\%$ and integral length scale, $L_I = 30$.

and the associated initial disturbance. The norm is intended to measure kinetic energy, and its square is defined as $\|\boldsymbol{q}\|^2 = \boldsymbol{q}^*\mathbf{L}^*\mathbf{L}\boldsymbol{q}$, where $\mathbf{L}^*\mathbf{L}$ is a positive-definite weight matrix, and $(\cdot)^*$ denotes Hermetian conjugation.

The statistical framework proposed by Ref. [18] instead considers the initial disturbance $\boldsymbol{q}(0,\beta,\omega)$ to be a random variable, and studies how the statistics of the evolved disturbance depend on those of the initial one. One quantity of particular importance is the expected disturbance energy downstream at a given wavenumber pair

$$\mathbb{E}[\|\boldsymbol{q}(x,\beta,\omega)\|^2] = \mathrm{Tr}\left(\mathbf{L}\boldsymbol{\Pi}(x,\beta,\omega)\mathbf{C}(0,\beta,\omega)\boldsymbol{\Pi}^*(x,\beta,\omega)\mathbf{L}^*\right). \tag{3}$$

Here, $\mathbf{C}(0,\beta,\omega) = \mathbb{E}[\boldsymbol{q}(0,\beta,\omega)\boldsymbol{q}^*(0,\beta,\omega)]$ is the two-point correlation of the initial upstream disturbances. The statistical analog of the optimal growth is the mean energy amplification G^{mean}, defined as the ratio of the expected energy downstream to that at the inlet. Using (3), this may be expressed as

$$G^{mean}(x,\beta,\omega) = \frac{\mathbb{E}[\|\boldsymbol{q}(x,\beta,\omega)\|^2]}{\mathbb{E}[\|\boldsymbol{q}(0,\beta,\omega)\|^2]} = \frac{\mathrm{Tr}\left(\mathbf{L}\boldsymbol{\Pi}(x,\beta,\omega)\mathbf{C}(0,\beta,\omega)\boldsymbol{\Pi}^*(x,\beta,\omega)\mathbf{L}^*\right)}{\mathrm{Tr}\left(\mathbf{L}\mathbf{C}(0,\beta,\omega)\mathbf{L}^*\right)}. \tag{4}$$

B. Inflow disturbance generation

Disturbances resembling freestream turbulence are imposed at the inflow station of the computational domain to study their evolution in the boundary layer. The method employed in the present work for generating these inflow perturbations closely follows approaches used in several prior studies, including investigations of free stream turbulence interaction with boundary layers [23, 24], disturbance growth on a NACA0008 airfoil subjected to free stream turbulence [25], DNS of turbulent pipe flow [26] and boundary layer transition in low-pressure turbine flows [27]. In this method, the velocity disturbances, denoted by $\boldsymbol{u'}$, are constructed as a superposition of Fourier modes,

$$\boldsymbol{u'}(\boldsymbol{x},t) = \sum_{\boldsymbol{\kappa}} \hat{\boldsymbol{u}}(\boldsymbol{\kappa}) \exp\left(i\boldsymbol{\kappa}\cdot\boldsymbol{x}\right) = \sum_{\boldsymbol{\kappa}=(\gamma,\beta,\omega)} \hat{\boldsymbol{u}}(\boldsymbol{\kappa}) \exp\left[i(\alpha x + \gamma y + \beta z)\right], \tag{5}$$

where $\hat{\boldsymbol{u}}(\boldsymbol{\kappa})$ denotes a random amplitude associated with the wavenumber vector $\boldsymbol{\kappa}$. To impose time-dependent disturbances at the inflow ($x = 0$), the streamwise phase term αx is replaced by $-\omega t$, effectively invoking Taylor's frozen turbulence hypothesis and neglecting the streamwise evolution of individual modes. The resulting perturbation field at the inlet takes the form

$$\boldsymbol{u'}(y,z,t;x=0) = \sum_{\gamma,\beta,\omega} \hat{\boldsymbol{u}}(\gamma,\beta,\omega) \exp\left[i(\gamma y + \beta z - \omega t)\right]. \tag{6}$$

Following the approach in Ref. [23], the three-dimensional Fourier amplitudes $\hat{\boldsymbol{u}}(\gamma,\beta,\omega)$ are prescribed to approximate a homogeneous and isotropic turbulence spectrum. Specifically, the von Kármán spectrum is employed, which is defined as

$$E(\kappa) = (\mathrm{TI})^2 \frac{L^5\kappa^4}{C[1+(\kappa L_I)^2]^{17/6}}, \tag{7}$$

where $\kappa = \sqrt{\gamma^2 + \beta^2 + \omega^2}$, TI denotes the turbulent intensity, L_I is a characteristic turbulent length scale, and

$$C = \frac{2}{3}\int_0^\infty \frac{x^4}{[1+x^2]^{17/6}}\mathrm{d}x \tag{8}$$

is a normalization constant that ensures that the prescribed energy spectrum yields the correct turbulent intensity. The von Kármán spectrum scales as κ^4 at large scales and transitions to the inertial range with a $\kappa^{-5/3}$ decay at small scales.

Before specifying the Fourier amplitudes in Eq. (6), we discuss the choice of key parameters, namely the integral length scale L_I and turbulence intensity TI, which influence the spectral content and amplitude of the imposed disturbances. Fig. 1 shows the energy spectrum for TI = 0.25% and $L_I = 30$. We select an integral length scale that is larger than those used in prior DNS studies of transition due to freestream disturbances imposed on the boundary layer [23, 24]. These studies focused on bypass transition and do not include freestream disturbances spanning the TS-wave spectral range. Using a larger integral length scale shifts the imposed disturbance spectrum toward lower frequencies, thereby allowing TS waves to be included. In addition, employing a low turbulence intensity ensures that any transient growth mechanisms produce low disturbance amplitudes over an extended streamwise region, thereby delaying the onset of nonlinear interactions and allowing TS-wave–driven linear growth to be clearly identified. DNS studies that investigate TS-wave growth [11, 12] have typically introduced disturbances in a controlled, narrow frequency band using localized forcing, such as a vibrating-ribbon–type boundary condition. In the present study, we impose a broadband spectrum of freestream disturbances, enabling the simultaneous excitation of TS-wave and non-modal mechanisms. To align our disturbance spectrum with prior TS-wave studies, the integral length scale is chosen based on the TS-wave forcing frequency used in Ref. [11].

Following the approach in Ref. [23], the Fourier mode amplitudes in Eq. (6) are prescribed in a form consistent with a homogeneous and isotropic turbulence spectrum. To account for the inherently random nature of turbulent fluctuations while preserving the prescribed spectral energy distribution, each Fourier mode is scaled by independent complex-valued stochastic coefficients. The resulting expressions for the Fourier amplitudes are

$$\hat{u} = \sqrt{\frac{E(\kappa)}{4\pi|\kappa|^4}}\left[z_1\frac{\gamma\omega}{\sqrt{\omega^2+\beta^2}} + z_2\beta\sqrt{\frac{\omega^2+\gamma^2+\beta^2}{\omega^2+\beta^2}}\right], \tag{9}$$

$$\hat{v} = -z_1\sqrt{\frac{E(\kappa)}{4\pi|\kappa|^4}}\sqrt{\omega^2+\beta^2}, \tag{10}$$

$$\hat{w} = \sqrt{\frac{E(\kappa)}{4\pi|\kappa|^4}}\left[z_1\frac{\gamma\beta}{\sqrt{\omega^2+\beta^2}} - z_2\omega\sqrt{\frac{\omega^2+\gamma^2+\beta^2}{\omega^2+\beta^2}}\right]. \tag{11}$$

Here, z_1 and z_2 are complex coefficients drawn from a standard normal distribution with zero mean and unit variance. When these coefficients are set to unity, $z_1 = z_2 = 1$, Eqs. (9-11) reduce exactly to the deterministic Fourier amplitudes proposed by Ref. [23]. These stochastic scalings ensure that the resulting perturbation field is not deterministic, but instead represents a statistically valid realization of synthetic freestream turbulence. This formulation captures the randomness inherent in turbulent flows while preserving key ensemble-averaged properties such as isotropy and spectral energy distribution consistent with the von Kármán spectrum. Although individual realizations of the velocity field may differ, ensemble-averaged quantities—such as turbulent kinetic energy and spectral content—converge to the target distribution upon averaging over multiple realizations. Importantly, incorporating the two independent complex coefficients—and no more—per mode ensures that the resulting velocity field in Fourier space lies in the subspace orthogonal to the wavenumber vector, thereby strictly satisfying the divergence-free condition. Including more than two coefficients would violate this divergence-free constraint. This approach facilitates the generation of a broadband disturbance field capable of exciting a wide range of instability modes in the boundary layer.

To incorporate the presence of the wall and satisfy the associated boundary conditions, the representation of the inflow disturbances in the wall-normal direction is modified. Specifically, the Fourier modes in the wall-normal direction y are replaced by an alternative form,

$$\boldsymbol{u'}(y,z,t;x=0) = \sum_{\gamma,\beta,\omega}\hat{\boldsymbol{u}}(\gamma,\beta,\omega)\zeta(y)\exp\left[i(\gamma y+\beta z-\omega t)\right], \tag{12}$$

where $\zeta(y)$ is a wall-normal shaping function applied to all velocity components. Its purpose is to ensure that the inflow velocity field perturbations satisfy the wall boundary conditions while producing a physically realistic wall-normal

distribution. In previous studies [23, 24, 27] that employ similar approaches for generating the inflow disturbances, the wall normal variation is constructed using Orr-Sommerfeld and Squire modes, which together form a complete basis for representing divergence-free perturbations. The present study does not utilize such a basis, since the primary objective is to compare the evolution of statistical flow quantities arising from a prescribed distribution of inflow disturbances at the inflow, as predicted by the fully nonlinear DNS and the statistical framework described in section II.A. In the present study, $\zeta(y)$ is chosen to increase rapidly from zero at the wall to unity in the free stream to provide a realistic wall-normal distribution of inflow perturbations and to then decay smoothly in the far field to avoid numerical reflections of disturbances at the far-field boundary. We select

$$\zeta(y) = \frac{1}{4}\tanh^2\left(\frac{y}{\delta_{yw}}\right)\left[1 - \tanh\left(\frac{y - y_f}{\delta_{yf}}\right)\right]^2 \tag{13}$$

as the wall-normal function for all velocity components with $\delta_{yw} = 0.2$, $\delta_{yf} = 2.5$, and $y_f = 50.0$.

C. One-way Navier-Stokes equations

Using the linearized Navier-Stokes equations to spatially evolve an initial disturbance downstream through the boundary layer is nominally ill-posed due to the presence of upstream-traveling waves. We use the one-way Navier-Stokes equations [7, 8, 19, 28], in which these upstream-traveling waves are removed, to obtain a well-posed spatial evolution operator. We begin by isolating the streamwise derivatives within the linearized Navier-Stokes equations, leading to an equation of the form

$$\mathbf{A}(x,\beta,\omega)\frac{\partial}{\partial x}\boldsymbol{q}(x,\beta,\omega) = -\left(i\omega\mathbf{I} + \mathbf{B}(x,\beta,\omega)\right)\boldsymbol{q}(x,\beta,\omega). \tag{14}$$

The primitive state variables are next transformed into the characteristic state space of the streamwise-dependent system. The discrete tensor $\mathbf{A}$ is diagonalizable and has real eigenvalues such that a transformation $\mathbf{T}$ exists such that

$$\mathbf{T}(x)\mathbf{A}(x,\beta,\omega)\mathbf{T}^{-1}(x) = \tilde{\mathbf{A}}(x,\beta,\omega) = \begin{bmatrix} \tilde{\mathbf{A}}_{++}(x,\beta,\omega) & 0 \\ 0 & \tilde{\mathbf{A}}_{--}(x,\beta,\omega) \end{bmatrix}, \tag{15}$$

where $\tilde{\mathbf{A}}$ contains the eigenvalues of $\mathbf{A}$, with positive characteristics $\tilde{\mathbf{A}}_{++} > 0$ and negative characteristics $\tilde{\mathbf{A}}_{--} < 0$. Similarly, the state vector $\boldsymbol{q}(x,\beta,\omega)$ can be transformed into characteristic space $\boldsymbol{\phi}(x,\beta,\omega) = \mathbf{T}(x)\boldsymbol{q}(x,\beta,\omega)$. For the march to be well-posed, upstream traveling waves must be removed from the evolution equation

$$\frac{\partial}{\partial x}\boldsymbol{\phi}(x,\beta,\omega) = \mathbf{M}(x,\beta,\omega)\boldsymbol{\phi}(x,\beta,\omega), \tag{16}$$

where $\mathbf{M} = -\tilde{\mathbf{A}}^{-1}\left(i\omega\mathbf{I} + \mathbf{T}\mathbf{B}\mathbf{T}^{-1} + \tilde{\mathbf{A}}\mathbf{T}\frac{\partial \mathbf{T}^{-1}}{\partial x}\right)$.

The exact parabolization can be determined using Briggs criterion [29] on the eigenvalues of $\mathbf{M}$ to isolate upstream and downstream traveling modes, which can be removed via the eigenexpansion of $\boldsymbol{\phi}$ into $\mathbf{M}$. The exact eigendecomposition of $\boldsymbol{\phi}$ and $\mathbf{M}$ is costly, so an approximation is made using a recursive differential-algebraic system,

$$\begin{aligned}
\boldsymbol{\phi}_-^{-N_\beta} &\approx \boldsymbol{\phi}_-^0, \\
\boldsymbol{\phi}_+^{-N_\beta} &= 0, \\
\left(\mathbf{M} - i\beta_-^{-j}\mathbf{I}\right)\boldsymbol{\phi}^{-j} &= \left(\mathbf{M} - i\beta_+^{j}\mathbf{I}\right)\boldsymbol{\phi}^{-j-1} \text{ for } j = 1, ..., N_\beta - 1, \\
\left(\mathbf{M} - i\beta_-^{0}\mathbf{I}\right)\boldsymbol{\phi}^{0} - \left(\mathbf{M} - i\beta_+^{0}\mathbf{I}\right)\boldsymbol{\phi}^{-1} &= \left(\mathbf{M} - i\beta_-^{0}\mathbf{I}\right)\boldsymbol{\phi}, \\
\left(\mathbf{M} - i\beta_+^{j}\mathbf{I}\right)\boldsymbol{\phi}^{j} &= \left(\mathbf{M} - i\beta_-^{j}\mathbf{I}\right)\boldsymbol{\phi}^{j+1} \text{ for } j = 0, ..., N_\beta - 1, \\
\boldsymbol{\phi}_-^{N_\beta} &= 0, \\
\boldsymbol{\phi}_+^{N_\beta} &\approx \boldsymbol{\phi}_+^0,
\end{aligned} \tag{17}$$

where β_+ and β_- are recursion parameters, generally chosen via rough knowledge of the local eigenspectra of $\mathbf{M}$. For simplicity, the one-way form of (16) can be represented as $\frac{\partial \boldsymbol{\phi}}{\partial x} = \mathbf{M}_+\boldsymbol{\phi} = \tilde{\mathbf{P}}\mathbf{M}\boldsymbol{\phi}$. The approximate projection tensor

$\tilde{\mathbf{P}}$ consists solely of approximations of the downstream traveling left eigenvectors of $\mathbf{M}$. Since $\tilde{\mathbf{P}}$ removes upstream traveling modes without altering downstream traveling modes, it is also applied to $\boldsymbol{\phi}$ after each streamwise step in the march. Further information on OWNS-P is provided in [19].

The final state $\boldsymbol{\phi}(x_f)$ can be represented as

$$\boldsymbol{\phi}(x_f) = \prod_{k=1}^{n_f} \exp\left[\tilde{\mathbf{P}}(x_k)\mathbf{M}(x_k)\Delta x\right] \boldsymbol{\phi}(0) \tag{18}$$

for $\Delta x \to 0$. Comparing with Eq. (1), the product of matrix exponentials in Eq. (18) constitutes the spatial propogator $\mathbf{\Pi}$. In practice, we do not explicitly form the matrix exponentials, instead advancing the solution using an appropriate integration scheme; here, we use a 4th-order backward difference scheme. The operator $\mathbf{M}$ is discretized using a 4th-order central difference scheme in the transverse direction with summation-by-parts closure. There are 2501 uniform streamwise stations and 151 transverse points with grid stretching [30] to increase resolution within the boundary layer. To ensure consistent physical representation across different frequencies, the downstream boundary is moved towards the inflow station proportionally to ω, leveraging the linear scaling of α with ω. An isothermal wall boundary condition is defined at the bottom of the domain, and an inviscid Thompson characteristic far-field boundary condition is applied at the top of the domain [31].

The initial disturbance $\boldsymbol{\phi}(0)$ can be a particular realization from DNS, outlined in section II.D, or generated by Gaussian white noise, outlined in section II.A. Since the process consists solely of linear transformations and using the knowledge that a Gaussian process undergoing linear transformations will remain Gaussian, the evolution of a set of realizations $\boldsymbol{q}(0,\beta,\omega) = \mathbf{B}z$, $z \sim N(0,1)$ and $z \in \mathbb{R}^{N_y,1}$, can be streamlined to reduce computation time. Instead, the eigenbasis of the Cholesky factorization matrix $\mathbf{B}(0,\beta,\omega)$ of $\mathbf{C}(0,\beta,\omega)$ is used as the set of initial conditions, and the sampling process is conducted downstream. This choice of initial basis reduces the number of initial conditions that need to be evolved, reducing cost when the number of realizations exceeds the number of wall-normal points.

D. Direct Numerical Simulations

In the present work, the fully nonlinear Navier-Stokes equations governing the flow of an incompressible viscous fluid are solved numerically. The governing equations for the velocity fields $\boldsymbol{u} = [u, v, w]$ in the Cartesian coordinates and pressure field p, written in the non-dimensional form, are

$$\frac{\partial \boldsymbol{u}}{\partial t} + (\boldsymbol{u}\cdot\nabla)\boldsymbol{u} = -\nabla p + \frac{1}{Re}\nabla^2\boldsymbol{u}, \tag{19}$$

$$\nabla\cdot\boldsymbol{u} = 0, \tag{20}$$

where Re denotes the Reynolds number based on the characteristic length and velocity scales. The characteristic length scale is chosen as as $\tilde{L}_{ref} = \sqrt{\tilde{\nu}\tilde{x}_0/\tilde{U}_\infty}$ where $\tilde{\cdot}$ denote dimensional quantities, $\tilde{\nu}$ is the kinematic viscosity, and $\tilde{x}_0$ is the distance from the leading edge. The free-stream velocity $\tilde{U}_\infty$ is chosen as the characteristic velocity scale. Accordingly, all spatial coordinates defining the computational domain are non-dimensionalized by $\tilde{L}_{ref}$. In the present study, Re is set to 300.0, which yields the Reynolds number based on the streamwise coordinate, i.e., $Re_x = \tilde{x}\tilde{U}_\infty/\tilde{\nu} = x\ Re$ at the inflow plane as $Re_{x_0} = 0.9\times10^5$.

Direct numerical simulations (DNS) are carried out using the open source Nek5000 [20] code, which is based on the spectral element method [32]. The governing equations are cast in weak form and discretized spatially using a Galerkin approximation, based on the $\mathbb{P}_N - \mathbb{P}_{N-2}$ formulation [33]. The velocity fields are approximated using Nth-order Lagrange polynomials defined on the Gauss-Lobatto-Legendre (GLL) points, while the pressure field is approximated using polynomials of order $N-2$ on Gauss-Legendre quadrature points. In all simulations presented in this work, a polynomial order of $N = 7$ is used. Time integration in Nek5000 is carried out using a high-order operator-splitting method: the viscous terms are treated implicitly using a third-order backward differentiation scheme, while the convective terms are advanced explicitly via an extrapolation method. Nek5000 offers high spatial and temporal accuracy through its high-order spectral element formulation, making it well-suited for resolving the full range of scales present in transitional and turbulent boundary layers. Parallelization is achieved through domain decomposition and message passing (MPI), allowing simulations to be conducted efficiently on high-performance computing clusters.

Fig. 2 shows a schematic of the flow domain used for the DNS computations in the present work. The domain extends from $300.0 \le x \le 2700.0$, $0.0 \le y \le 120.0$, and $0.0 \le z \le 60.0$ in the streamwise, wall-normal, and spanwise directions, respectively. The streamwise domain length is chosen long enough to capture a sufficient region of growth

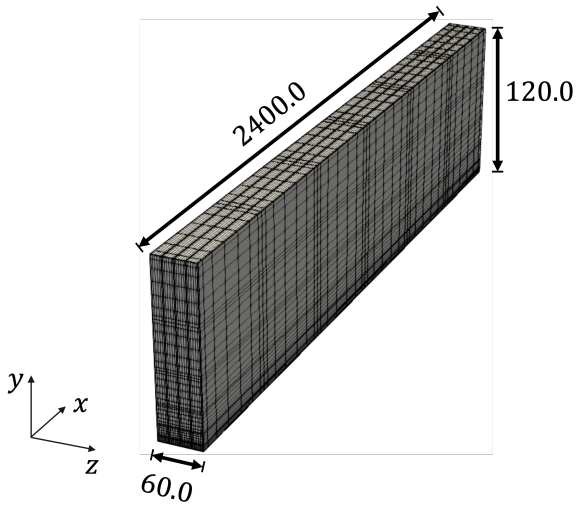

Fig. 2 Schematic of the DNS computational domain. The mesh spacing shown is for illustration only.

of the imposed perturbations. Inflow perturbations are superimposed at the inlet station ($x = 0$), and the method for generating these disturbances is described in section II.B. A Dirichlet boundary condition is imposed at the inlet, corresponding to the Blasius profile with a boundary layer thickness of $\delta_{99} \approx 4.9$, onto which the perturbations are imposed. At the downstream boundary, a zero-gradient outflow condition ($\nabla \boldsymbol{u} = 0$) is applied. In the wall-normal direction, no-slip and no-penetration conditions are imposed at the wall ($y = 0$), and a stress-free Neumann-type condition is imposed at the top boundary ($y = 120.0$). Periodic boundary conditions are applied in the homogeneous spanwise direction.

The computational mesh consists of $256 \times 64 \times 16$ spectral elements along the x, y, and z directions, respectively, resulting in approximately 91 million grid points. The mesh distribution shown in Fig. 2 is for illustration only and does not reflect the actual computational mesh. The mesh employs clustering of grid points near the wall to accurately resolve the boundary layer and its transition. The minimum grid spacing in the wall-normal direction is $\Delta y \sim 0.36$. The computational non-dimensional time step is fixed at $\Delta t = 1.25 \times 10^{-2}$, corresponding to a Courant-Friedrichs-Lewy (CFL) number ~ 0.35, based on the minimum wall-normal grid spacing and freestream velocity.

The perturbations are evolved from the initial state for $4 \times 10^5 \Delta t$, which corresponds to $\approx 2.1 t_f$, where t_f denotes the flow-through time of the computational domain, defined based on the streamwise extent of the domain and the free-stream velocity. This evolution allows the flow to reach a statistically stationary state. The DNS is then continued for an additional 10^6 time steps, during which the instantaneous flow fields are sampled every $200\Delta t$, yielding a total of 5,000 samples. To reduce memory requirements and computational cost in the subsequent analysis while retaining the energetic flow features of interest, the solution is downsampled in the streamwise direction by a factor of 15, reducing the number of grid points from 1793 to 120. To obtain frequency-domain modes from the time-series data, the data are divided into 24 overlapping blocks, with a 50% overlap between consecutive blocks and 400 samples per block, resulting in a frequency resolution of $\Delta\omega = 0.0063$.

III. Results and discussion

We first present results from DNS of the Blasius boundary layer with free-stream disturbances imposed at the inflow of the computational domain. Fig. 3 shows the evolution of the streamwise velocity perturbation field, u', obtained by subtracting the Blasius base flow from the instantaneous velocity field. Results are shown at wall-normal locations $y = 6.0$ (left) and $y = 10.6$ (right) from the plate, at four time instances. The first snapshot corresponds to $t \approx 0.26 t_f$, with successive snapshots separated by approximately $0.5 t_f$. A qualitative comparison of the left and right panels reveals significantly larger perturbation growth near the wall ($y = 6.0$), as expected. Moreover, the evolution of u' at this location indicates selective amplification in the spanwise spectral space. Although broadband disturbances are imposed over a wide range of spanwise wavenumbers β, Fig. 3 shows that only a subset of wavenumbers undergo significant

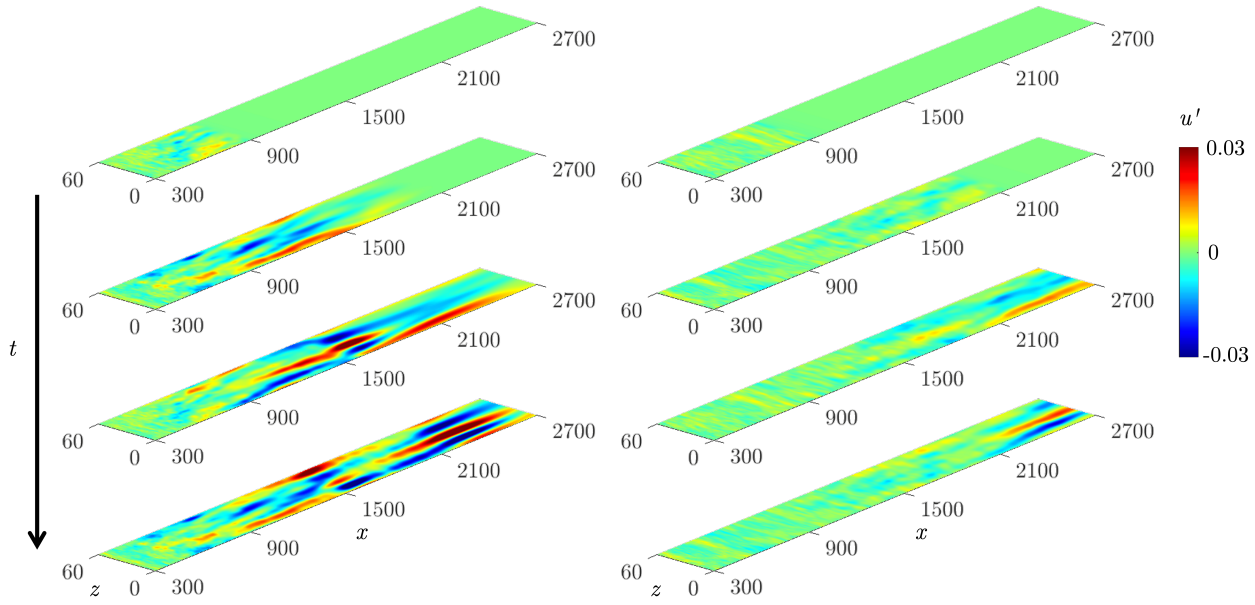

Fig. 3 Streamwise velocity fluctuation u' at wall-normal distances of $y = 6.0$ (left panel) and $y = 10.6$ (right panel) from the plate, shown at four time instances. The first snapshot corresponds to $t \approx 0.26t_f$ and the time interval between successive snapshots is $\approx 0.5t_f$.

amplification. This observation justifies our focus on quantifying disturbance growth independently for distinct (ω, β) pairs.

To examine the linear streamwise evolution predicted by OWNS, we first compare DNS and OWNS solutions for a single realization. Figs. 4 (a) and (b) show the real part of the streamwise velocity perturbation, $\hat{u}$, for the Fourier mode with $\omega = 0.0251$ and $\beta = 0.0$, obtained from DNS and OWNS, respectively. The DNS result (Fig. 4 (a)) is computed using a long-time Fourier transform, i.e., without segmenting the time series into blocks prior to performing the FFT. Both DNS and OWNS solutions are normalized by the corresponding complex value of $\hat{u}$ at $x = 2200$ and $y = 1.5$, thereby removing the arbitrary phase of the Fourier mode. The black solid curve overlaid on each figure denotes the laminar Blasius boundary-layer thickness, δ_{99}, and this representation is used consistently throughout the paper to indicate the laminar boundary-layer thickness.

Despite differences in the wall-normal structure of the imposed disturbances, reflected by the differing perturbation amplitudes in the free stream at the inflow ($x = 300.0$), the evolution of the perturbation field within the boundary layer shows good qualitative agreement between DNS and OWNS. Figs. 4 (a) and (b) further show that the freestream perturbations, i.e., away from the wall, are advected downstream with negligible growth or decay in amplitude in both DNS and OWNS solutions, respectively. The associated streamwise wavenumber for these structures, as annotated in the figures, is $\alpha \approx \omega$, consistent with Taylor's frozen turbulence hypothesis used to construct the inflow perturbations. Within the boundary layer, however, the perturbation amplitudes exhibit significant growth, with the corresponding structures characterized by $\alpha > \omega$. To isolate these growing boundary layer structures, we apply a high-pass filter in the streamwise spectral space, retaining perturbations with $\alpha/\omega \geq 1.25$. The filtered results, shown in Figs. 4 (c) and (d), demonstrate good agreement between DNS and OWNS. Although not shown here, the other velocity components exhibit a similar level of agreement. The associated phase speed of these structures is $\omega/\alpha \approx 0.4$, consistent with that of a TS wave, as reported in Ref. [3], and these results therefore establish a basis to extend the analysis to multiple realizations to examine mean energy growth and validate the proposed statistical framework.

Next, we examine multiple DNS realizations to illustrate the variability in the boundary layer response. The time-series data is segmented into overlapping blocks, as described in section II.D, with each block treated as an approximately uncorrelated realization. Figs. 5 (a) and (b) show two such realizations of $\hat{u}$ for the $(\omega, \beta) = (0.0251, 0.1047)$ Fourier mode. While the freestream perturbations are simply advected downstream, the boundary layer response exhibits noticeable differences in amplitude, structure, and the location of maximum amplification across realizations, highlighting the sensitivity of perturbation growth to specific inflow conditions. This variability is further emphasized

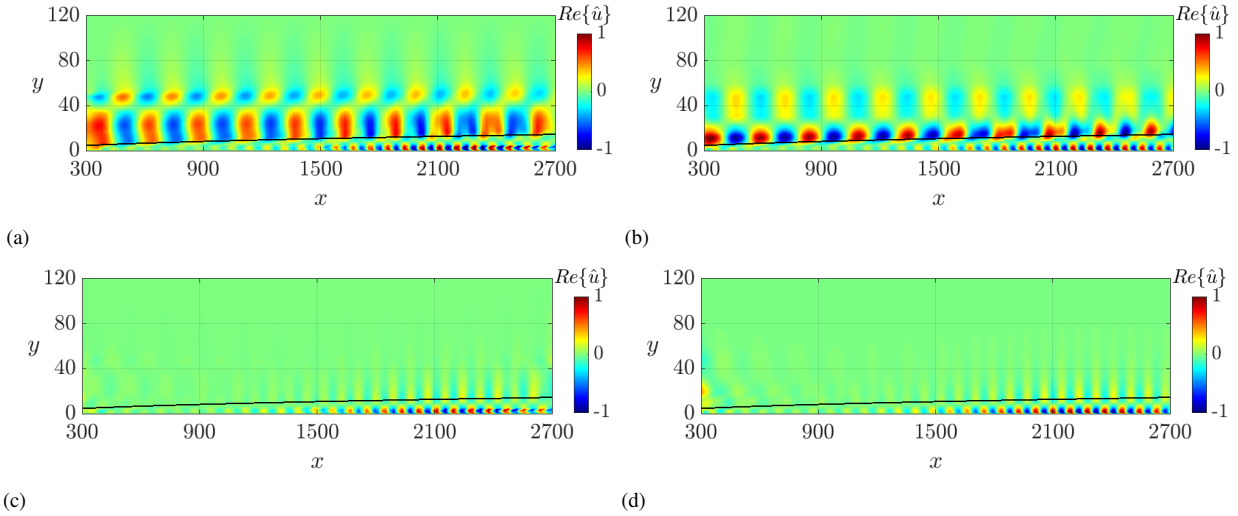

Fig. 4 Comparison of the real part of the streamwise velocity perturbation, $\hat{u}$ for $\omega = 0.0251$ and $\beta = 0.0$, for a single realization obtained from (a) DNS and (b) OWNS. The black solid curve denotes the initial Blasius boundary layer thickness δ_{99}. Figures (c) and (d) show the same fields after applying a high-pass filter in the streamwise spectral space to isolate the structures amplifying within the boundary layer.

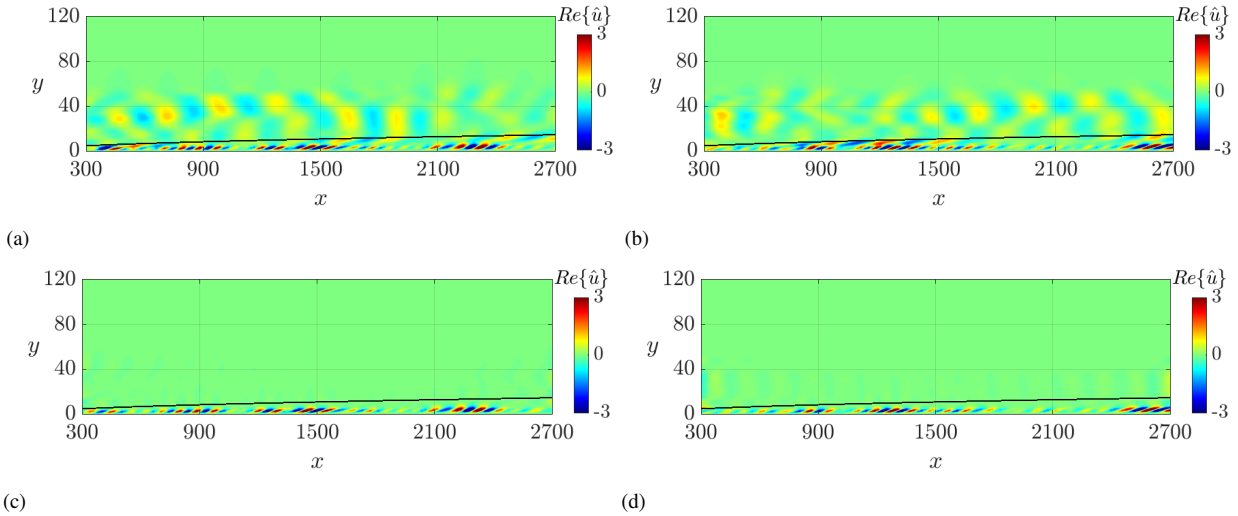

Fig. 5 (a) and (b) show the streamwise velocity perturbation, $\hat{u}$, for $(\omega, \beta) = (0.0251, 0.1047)$ from two DNS realizations. (c) and (d) show the corresponding streamwise-filtered boundary layer structures.

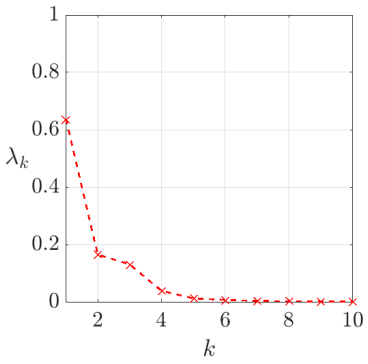

Fig. 6 Eigenvalue (λ_k) spectrum of the inflow correlation matrix for $(\omega, \beta) = (0.0251, 0.1047)$, normalized by the total inflow energy.

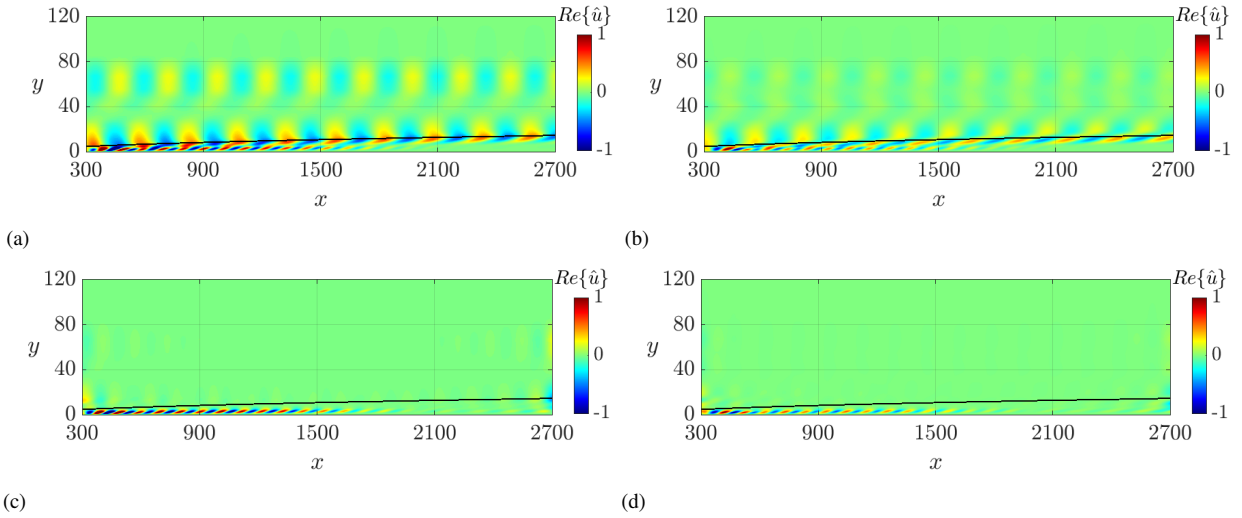

Fig. 7 Streamwise velocity perturbation, $\hat{u}$, for $(\omega, \beta) = (0.0251, 0.1047)$, spatially marched downstream using OWNS. (a) and (b) correspond to the eigenvectors associated with the first and third eigenvalues of the inflow correlation matrix (see Fig. 6), while (c) and (d) show the corresponding streamwise-filtered boundary layer structures.

in Figs. 5 (c) and (d), which isolate the growing boundary layer structures corresponding to realizations (a) and (b), respectively. Such differences motivate the use of a statistical framework, in which the energy is averaged over multiple realizations to compute the mean energy growth.

Following the DNS analysis, we next examine the evolution of boundary layer disturbances using the proposed reduced-order statistical framework. In this approach, a subset of the most energetic eigenvectors of the inflow correlation matrix is marched downstream using OWNS, providing an efficient means to capture the mean growth of perturbation energy without simulating all inflow realizations individually. Fig. 6 shows the eigenvalues of the inflow correlation matrix for $(\omega, \beta) = (0.0251, 0.1047)$, normalized by the total energy imposed at the corresponding (ω, β) pair. Figs. 7 (a) and (b) show the streamwise evolution of the eigenvectors corresponding to the first and third eigenvalues in Fig. 6, while Figs. 7 (c) and (d) show the corresponding streamwise filtered fields. As expected, the perturbation structures within the boundary layer grow significantly, while the freestream structures are merely advected downstream. Although only the first few eigenvalues are significant as evident from Fig. 6, eigenvectors associated with smaller eigenvalues may still grow downstream and contribute to the boundary layer dynamics. Therefore, we retain for downstream marching all eigenvectors with eigenvalues greater than 10^{-8}. For the (ω, β) pairs analyzed in this study, this corresponds to approximately 50-60 eigenvectors.

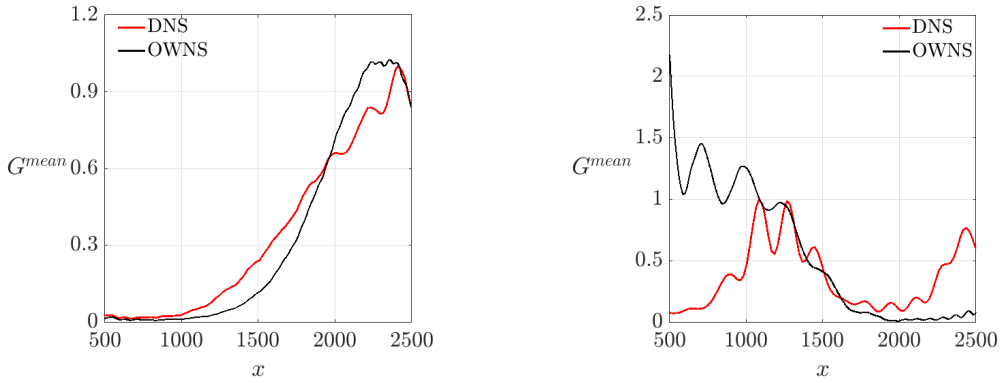

Fig. 8 Mean energy growth comparison between DNS and OWNS-based statistical framework for (a) $(\omega, \beta) = (0.0251, 0.0)$ **(b)** $(\omega, \beta) = (0.0251, 0.1047)$**. The mean energy growth is normalized by its corresponding value at the streamwise location where DNS exhibits peak growth.**

The reduced-order statistical framework enables efficient computation of the mean energy growth across the boundary layer by evolving a limited set of eigenvectors of the inflow correlation matrix. In the present study, to enable a meaningful quantitative comparison with DNS, two practical considerations must be accounted for. First, the evolved flow fields are spectrally filtered in the streamwise direction to isolate the boundary layer structures, which introduces spurious values near the streamwise boundaries of the domain. Second, the OWNS formulation requires projection of the inflow perturbations onto the downstream-traveling subspace, thereby removing contributions associated with upstream-traveling modes. As a result, direct comparison of mean energy growth along the entire streamwise extent is not meaningful. We therefore compare the mean energy growth normalized by its value at the streamwise location where the DNS exhibits maximum energy for a given (ω, β) pair, enabling a consistent assessment of the streamwise evolution of disturbance energy between DNS and the reduced-order OWNS-based statistical framework. The quantitative differences arising from the projection and removal of energy associated with the upstream-traveling components will be addressed systematically in future work.

Fig. 8 presents a comparison of the mean energy growth predicted by DNS and the reduced-order OWNS-based statistical framework for (a) $(\omega, \beta) = (0.0251, 0.0)$ and (b) $(\omega, \beta) = (0.0251, 0.1047)$. In each case, the mean energy growth is normalized by its value at the streamwise location where the DNS exhibits maximum mean energy growth. For $(\omega, \beta) = (0.0251, 0.0)$, Fig. 8 (a) shows good agreement in the streamwise variation of G^{mean} between DNS and OWNS. In contrast, Fig. 8 (b) shows noticeable discrepancies for $(\omega, \beta) = (0.0251, 0.1047)$. This mismatch is associated with the fact that this mode undergoes substantial amplification very close to the inflow plane, as evident from Figs. 5 and 7. Since the OWNS formulation involves projection onto the downstream-traveling subspace and the comparison employs streamwise spectral filtering, the largest differences between DNS and OWNS are expected in regions close to the inflow boundary.

In contrast, for modes whose dominant growth occurs sufficiently far downstream, as in Fig. 8(a) and as illustrated in Fig. 4, the OWNS-based statistical framework reproduces the mean energy growth trends observed in DNS. These results demonstrate that the proposed framework provides a consistent and efficient means of capturing mean disturbance growth, while highlighting practical considerations associated with inflow treatment and streamwise filtering that influence the interpretation of normalized energy comparisons. For modes such as $(\omega, \beta) = (0.0251, 0.1047)$, quantitative differences may also arise due to interactions with other (ω, β) pairs not accounted for in the linear reduced-order framework. A systematic treatment of inflow projection effects and streamwise filtering will be pursued in future work, while interactions among multiple (ω, β) modes will be addressed using a nonlinear implementation of OWNS.

IV. Conclusions

This paper investigates the statistical modeling of disturbance growth in the spatially developing Blasius boundary layer using a linear implementation of the one-way Navier–Stokes (OWNS) method. Fully nonlinear direct numerical

simulations (DNS), with free-stream disturbances imposed at the inflow, serve as a benchmark for assessing the predictions of the proposed framework. We have introduced a reduced-order statistical approach that efficiently computes the mean growth of boundary-layer disturbances by marching a subset of eigenvectors of the inflow correlation matrix using linear OWNS. Comparisons with DNS across multiple (ω, β) pairs demonstrate that the framework accurately captures the evolution of perturbation structures and mean energy growth within the boundary layer. While practical factors, such as inflow projection and streamwise filtering, can influence quantitative comparisons near the inflow, the method provides a robust, computationally efficient tool for analyzing transition-relevant disturbances. A systematic treatment of inflow projection, streamwise filtering, and interactions among multiple (ω, β) modes will be pursued in future work, with the latter addressed through a nonlinear implementation of OWNS.

Acknowledgments

This work was funded in part by ONR grant no. N00014-24-1-2033. We would like to thank Dr. Tim Colonius for the use of the OWNS implementation within the Caltech Stability and Transition Analysis Toolkit (CSTAT).

References

[1] Reshotko, E., "Boundary-Layer Stability and Transition," *Annual Review of Fluid Mechanics*, Vol. 8, No. Volume 8, 1976, 1976, pp. 311–349. https://doi.org/https://doi.org/10.1146/annurev.fl.08.010176.001523.

[2] Herbert, T., "Secondary Instability of Boundary Layers," *Annual Review of Fluid Mechanics*, Vol. 20, No. Volume 20, 1988, 1988, pp. 487–526. https://doi.org/https://doi.org/10.1146/annurev.fl.20.010188.002415.

[3] Schmid, P., and Henningson, D., *Stability and Transition in Shear Flows*, Vol. 142, 2001. https://doi.org/10.1007/978-1-4613-0185-1.

[4] Reed, H. L., Saric, W. S., and Arnal, D., "Linear Stability Theory Applied to Boundary Layers," *Annual Review of Fluid Mechanics*, Vol. 28, No. Volume 28, 1996, 1996, pp. 389–428. https://doi.org/https://doi.org/10.1146/annurev.fl.28.010196.002133.

[5] Herbert, T., "Parabolized stability equations," *Annual Review of Fluid Mechanics*, Vol. 29, No. Volume 29, 1997, 1997, pp. 245–283. https://doi.org/https://doi.org/10.1146/annurev.fluid.29.1.245.

[6] Towne, A., Rigas, G., and Colonius, T., "A critical assessment of the parabolized stability equations," *Theoretical and Computational Fluid Dynamics*, Vol. 33, No. 3–4, 2019, p. 359–382. https://doi.org/10.1007/s00162-019-00498-8.

[7] Towne, A., and Colonius, T., "Continued development of the one-way Euler equations: Application to Jets," *20th AIAA/CEAS Aeroacoustics Conference*, 2014. https://doi.org/10.2514/6.2014-2903.

[8] Towne, A., and Colonius, T., "One-way spatial integration of hyperbolic equations," *Journal of Computational Physics*, Vol. 300, 2015, p. 844–861. https://doi.org/10.1016/j.jcp.2015.08.015.

[9] Sleeman, M. K., Colonius, T., and Lakebrink, M. T., "Boundary-layer stability analysis using the nonlinear one-way navier–stokes approach," *AIAA Journal*, 2025, p. 1–15. https://doi.org/10.2514/1.j064909.

[10] Spalart, P. R., "Direct simulation of a turbulent boundary layer up to R = 1410," *Journal of Fluid Mechanics*, Vol. 187, 1988, p. 61–98. https://doi.org/10.1017/S0022112088000345.

[11] Rist, U., and Fasel, H., "Direct numerical simulation of controlled transition in a flat-plate boundary layer," *Journal of Fluid Mechanics*, Vol. 298, 1995, pp. 211–248. https://doi.org/https://doi.org/10.1017/S0022112095003284.

[12] Wu, X., and Moin, P., "Direct numerical simulation of turbulence in a nominally zero-pressure-gradient flat-plate boundary layer," *Journal of Fluid Mechanics*, Vol. 630, 2009, p. 5–41. https://doi.org/10.1017/S0022112009006624.

[13] Matsubra, M., and Alfredsson, P. H., "Disturbance growth in boundary layers subjected to free-stream turbulence," *Journal of Fluid Mechanics*, Vol. 430, 2001, p. 149–168. https://doi.org/10.1017/S0022112000002810.

[14] Brandt, L., "The lift-up effect: The linear mechanism behind transition and turbulence in shear flows," *European Journal of Mechanics - B/Fluids*, Vol. 47, 2014, pp. 80–96. https://doi.org/https://doi.org/10.1016/j.euromechflu.2014.03.005, enok Palm Memorial Volume.

[15] Butler, K. M., and Farrell, B. F., "Three-dimensional optimal perturbations in viscous shear flow," *Physics of Fluids A: Fluid Dynamics*, Vol. 4, No. 8, 1992, pp. 1637–1650. https://doi.org/10.1063/1.858386.

[16] Trefethen, L. N., Trefethen, A. E., Reddy, S. C., and Driscoll, T. A., "Hydrodynamic Stability Without Eigenvalues," *Science*, Vol. 261, No. 5121, 1993, pp. 578–584. URL http://www.jstor.org/stable/2882016.

[17] Saric, W. S., Reed, H. L., and Kerschen, E. J., "Boundary-layer receptivity to freestream disturbances," *Annual Review of Fluid Mechanics*, Vol. 34, No. Volume 34, 2002, 2002, pp. 291–319. https://doi.org/https://doi.org/10.1146/annurev.fluid.34.082701.161921.

[18] Frame, P., and Towne, A., "Beyond optimal disturbances: a statistical framework for transient growth," *Journal of Fluid Mechanics*, Vol. 983, 2024. https://doi.org/10.1017/jfm.2024.100.

[19] Towne, A., Rigas, G., Kamal, O., Pickering, E., and Colonius, T., "Efficient global resolvent analysis via the one-way navier–stokes equations," *Journal of Fluid Mechanics*, Vol. 948, 2022. https://doi.org/10.1017/jfm.2022.647.

[20] Fischer, P. F., Lottes, J. W., and Kerkemeier, S. G., "Nek5000: open source spectral element CFD solver. Argonne National Laboratory, Mathematics and Computer Science Division." , 2008. URL https://nek5000.mcs.anl.gov/.

[21] Reddy, S. C., and Henningson, D. S., "Energy growth in viscous channel flows," *Journal of Fluid Mechanics*, Vol. 252, 1993, p. 209–238. https://doi.org/10.1017/S0022112093003738.

[22] Schmid, P. J., "Nonmodal Stability Theory," *Annual Review of Fluid Mechanics*, Vol. 39, No. 1, 2007, pp. 129–162. https://doi.org/10.1146/annurev.fluid.38.050304.092139.

[23] Jacobs, R. G., and Durbin, P. A., "Simulations of bypass transition," *Journal of Fluid Mechanics*, Vol. 428, 2001, p. 185–212. https://doi.org/10.1017/S0022112000002469.

[24] Brandt, L., Schlatter, P., and Henningson, D. S., "Transition in boundary layers subject to free-stream turbulence," *Journal of Fluid Mechanics*, Vol. 517, 2004, p. 167–198. https://doi.org/10.1017/S0022112004000941.

[25] Faúndez Alarcón, J. M., Morra, P., Hanifi, A., and Henningson, D. S., "Disturbance growth on a NACA0008 wing subjected to free stream turbulence," *Journal of Fluid Mechanics*, Vol. 944, 2022, p. A44. https://doi.org/10.1017/jfm.2022.506.

[26] El Khoury, G. K., Schlatter, P., Noorani, A., Fischer, P. F., Brethouwer, G., and Johansson, A. V., "Direct numerical simulation of turbulent pipe flow at moderately high Reynolds numbers," *Flow, turbulence and combustion*, Vol. 91, 2013, pp. 475–495. https://doi.org/https://doi.org/10.1007/s10494-013-9482-8.

[27] Đurović, K., De Vincentiis, L., Simoni, D., Lengani, D., Pralits, J., Henningson, D. S., and Hanifi, A., "Free-Stream Turbulence-Induced Boundary-Layer Transition in Low-Pressure Turbines," *Journal of Turbomachinery*, Vol. 143, No. 8, 2021, p. 081015. https://doi.org/10.1115/1.4050450.

[28] Zhu, M., and Towne, A., "Recursive one-way navier-stokes equations with PSE-like cost," *Journal of Computational Physics*, Vol. 473, 2023, p. 111744. https://doi.org/10.1016/j.jcp.2022.111744.

[29] Briggs, R. J., "Beam-plasma interactions in a one- dimensional system," *Electron-Stream Interaction with Plasmas*, 1964, p. 47–83. https://doi.org/10.7551/mitpress/2675.003.0005.

[30] Malik, M., "Numerical methods for hypersonic boundary layer stability," *Journal of Computational Physics*, Vol. 86, No. 2, 1990, p. 376–413. https://doi.org/10.1016/0021-9991(90)90106-b.

[31] Thompson, K. W., "Time dependent boundary conditions for hyperbolic systems," *Journal of Computational Physics*, Vol. 68, No. 1, 1987, p. 1–24. https://doi.org/10.1016/0021-9991(87)90041-6.

[32] Patera, A. T., "A spectral element method for fluid dynamics: Laminar flow in a channel expansion," *Journal of Computational Physics*, Vol. 54, No. 3, 1984, pp. 468–488. https://doi.org/https://doi.org/10.1016/0021-9991(84)90128-1.

[33] Maday, Y., and Patera, A. T., "Spectral element methods for the incompressible Navier-Stokes equations," *IN: State-of-the-art surveys on computational mechanics (A90-47176 21-64). New York*, 1989, pp. 71–143. URL https://ntrs.nasa.gov/citations/19900060124.